Developing ductile and isotropic Ti alloy with tailored composition for laser powder bed fusion

Leyun Wang[1,5,6*], Zhe Song[1], Xuan Zhang[2], Jun-Sang Park[3], Jonathan Almer[3], Gaoming Zhu[1], Yiwen Chen[1], Quan Li[1], Xiaoqin Zeng[1], Yanjun Li[4]

[1] *National Engineering Research Center of Light Alloy Net Forming, Shanghai Jiao Tong University, Shanghai 200240, China*

[2] *Nuclear Science and Engineering Division, Argonne National Laboratory, Lemont, IL 60439, USA*

[3] *Advanced Photon Source, Argonne National Laboratory, Lemont, IL 60439, USA*

[4] *Department of Materials Science and Engineering, Norwegian University of Science and Technology, Trondheim 7491, Norway*

[5] *State Key Laboratory of Metal Matrix Composites, Shanghai Jiao Tong University, Shanghai 200240, China*

[6] *Additive Manufacturing Research Center, School of Materials Science and Engineering, Shanghai Jiao Tong University, Shanghai 200240, China*

* corresponding author: leyunwang@sjtu.edu.cn

Abstract

Laser powder bed fusion (LPBF) is an advanced technology to create metallic components with complex geometry. Ti-6Al-4V (Ti64) is one of the most frequently used materials for LPBF. The intrinsic high cooling rates and ultra-high directional thermal gradient of melt, however, lead to a hierarchical structure composed of fine martensitic α' within columnar prior-β grains in LPBF Ti64. This microstructure results in poor ductility and strong mechanical anisotropy in as-built Ti64 components, which largely limit their applications. Here, we report that the above shortcomings can be

overcome by tailoring the alloy composition. Specifically, by reducing the aluminum content from 6wt.% to 4wt.%, the resultant LPBF Ti-4Al-4V (Ti44) alloy exhibits substantially improved ductility and mechanical isotropy. These improvements are attributed to grain refinement during solidification and the activation of multiple slip modes and twinning in the as-built material during deformation. This work offers a simple strategy to design new titanium alloys for LPBF with significantly improved ductility and isotropy.

Keywords: Titanium alloys; Laser powder bed fusion; Grain refinement; Ductility; Synchrotron diffraction

1. Introduction

Additive manufacturing (AM) produces three-dimensional objects by stacking thin layers of materials based on a digital model. While AM is versatile in the choice of materials, its biggest market lies in fabricating metal components for high-end applications [1]. Laser powder bed fusion (LPBF) is a very popular AM process for metals. It uses a fine laser beam to selectively fuse regions of a metal powder bed to build the component layer-by-layer. So far, a key challenge for the industrial use of LPBF is how to ensure that the components made by this technology would have properties that are comparable to their counterparts made by traditional manufacturing processes. Due to the ultra-high thermal gradient during laser fusion, LPBF metals often display unique microstructures. Ti64 (Ti-6Al-4V, wt.%) is one of the most frequently

used materials for LPBF. LPBF Ti64 features a hierarchical structure of acicular martensitic α' needles within columnar prior-β grains [2, 3], which is drastically different from the two-phase α+β microstructures (fully lamellar, bi-modal, or fully equiaxed) typically found in this material [4]. Compared to Ti64 made by traditional manufacturing processes (i.e. casting, homogenization, deformation, recrystallization, annealing), LPBF Ti64 usually exhibit lower tensile ductility (fracture elongation, $\varepsilon_f \leq$ 10%) and strong mechanical anisotropy with respect to the building direction (BD) [5–8]. These issues significantly limit the usage of LPBF Ti64 in the aerospace industry (the biggest consumer of titanium), which has stringent safety standards.

Post-processing heat treatment can increase the ductility of LPBF Ti64, as the brittle α' phase would decompose into a two-phase α+β microstructure under elevated temperatures. The mechanical anisotropy, however, is still unavoidable because heat treatment usually does not alter the columnar grain structure [8]. Besides, heat treatment increases the overall processing time and the manufacturing cost. Some recent works proposed a few new strategies to enhance the ductility of LPBF Ti64 by either reducing the scan speed or/and the hatch spacing in order to trigger in-situ α' decomposition during the building process [9–12], or applying more sophisticated post-processing heat treatment routes to modify the columnar grain structure [13, 14]. While those strategies can produce materials with higher ductility (ε_f: 15%–25%), implementing such strategies requires even longer processing time, which ultimately makes the products prohibitively expensive.

Compared to post-processing heat treatment or tweaking the building parameters, designing new titanium alloys specifically for LPBF is a more challenging but also more rewarding research direction. For example, it has been shown that the addition of alloying elements (via either powder mixing or pre-alloying) such as boron [15], tungsten [16], copper [17], and iron [18] can restrict the growth of columnar prior-β grains after laser fusion. This solute-induced grain refinement increases the material strength [19, 20], but the material ductility is often further sacrificed owing to the formation of brittle intermetallic compounds [15, 17].

In the present work, we report that the microstructure and mechanical properties of AM titanium alloys can be engineered by simply adjusting the aluminum (Al) content in Ti-Al-V alloys. Al is the most common alloying element in Ti alloys. It is known as an α stabilizer that raises the β→α transition temperature for titanium, and it has large solubility in both α and β phases [4].

As a substitutional solute in α-Ti's hexagonal lattice, Al provides the solution hardening effect by introducing obstacles to dislocation glide. Earlier works have shown that Al provides stronger strengthening on prismatic slip (the easiest slip mode in α-Ti) than on basal slip (the second easiest slip mode in α-Ti) [21]. A proper Al content can theoretically equal the critical resolved shear stress (CRSS) of prismatic slip and basal slip. Recent electron microscopy studies indicate that Al solutes exist in Ti's lattice

within short-range ordered (SRO) domains in a DO_{19} (Ti_3Al) pattern [22]. When interacting with dislocations, the SRO domains cause “wavy to planar” slip transition, leading to localized planar deformation and, consequently, lower ductility. Due to the ultra-fast solidification in LPBF, Al solutes in LPBF Ti alloys may or may not affect dislocation activity as they do in hot-processed Ti alloys. In the present work, we study the influence of Al content on the mechanical properties of LPBF Ti alloys. In particular, we will show that a moderate reduction of Al weight percentage from 6% to 4% in the Ti-*x*Al-4V alloy system can significantly improve the ductility and isotropy at the expense of reduced strength. The origins of the change in mechanical properties will be explored from quantitative microstructure characterization, *in situ* synchrotron X-ray diffraction experiments, and solidification theory.

2. Material and experimental procedures

Pure Ti (99.9%), pure Al (99.9%), and an Al-58wt.% V master alloy were melted in a vacuum arc remelting (VAR) furnace to fabricate a cast billet with the nominal composition of Ti44 (Ti-4Al-4V, wt.%). The billet was forged and machined to produce a cylindrical ingot with a diameter of 50 mm. The ingot was remelted and atomized into powders using an ALD EIGA 50-500 equipment. The heating power, material feed rate, and air pressure for the gas atomization were 20~40 kW, 40~60 mm/min, and 3.5~4.5 MPa, respectively. The obtained Ti44 powder shows good sphericity, with diameter ranging from 5.5 to 124.5 μm (mean value = 34.6 μm), as measured by a laser diffraction particle size analyzer (Microtrac S3500) and shown in Fig. 1. Table 1 shows

the chemical composition of the powder, as measured by an inductively coupled plasma atomic emission spectroscopy (ICP-AES) analyzer (Perkin-Elmer, Plasma 400). The chemical composition of the powder was close to the designed composition.

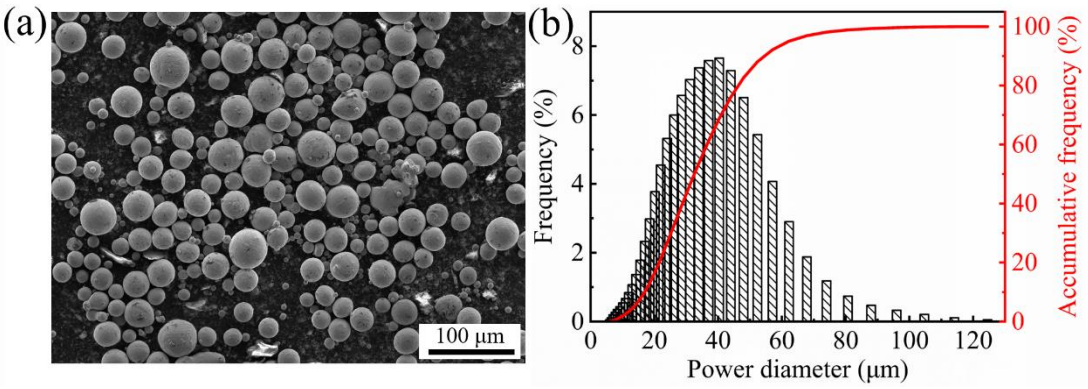

Fig. 1. Characterization of the Ti44 powder. (a) Scanning electron microscope image. (b) Powder size distribution measured by a Microtrac S3500 instrument.

Table 1. Chemical composition of the Ti44 powder, as-built Ti44 and Ti64 bars.

	Element (wt.%)							
	Al	V	Fe	C	N	H	O	Ti
Ti44/powder	3.89	3.61	0.020	0.007	0.0016	0.0008	0.090	bal
Ti44/as-built	3.80	3.94	0.026	0.0096	0.017	0.0016	0.112	bal
Ti64/as-built	5.87	3.99	0.21	0.0088	0.011	0.0022	0.087	bal

The Ti44 powder was screened for 15~53 μm in diameter. The size distribution after screening was measured: D10=17 μm, D50=33 μm, D90=54 μm. The powder was loaded into an EOSINT M280 SLM machine for LPBF processing with the following building parameters: laser power = 280 W, scan speed = 1200 mm/s, hatch spacing =

140 μm, layer thickness = 30 μm, substrate preheating temperature = 100 ℃. The scan path was rotated by 67° between each layer. The above parameters were adopted from the building of Ti64 components. Two sets of bulk bars with the dimension of 12×12×80 mm^3 were built, whose longitudinal axes were parallel or perpendicular to the BD, respectively. Those bars were named as Ti44-V (vertical) or Ti44-H (horizontal). For comparison, a Ti64-V bar (longitudinal axis parallel to BD) and a Ti64-H bar (longitudinal axis perpendicular to BD) were also fabricated using commercial Ti-6Al-4V powders under the same building parameters. The chemical compositions of the as-built Ti44 and Ti64 bars were also measured by ICP-AES and shown in Table 1. For Ti44, the LPBF process does not significantly change its chemistry from the powder.

Optical Microscopy (Zeiss Axio Vert. A1) was conducted to examine the defects in the as-built materials. Electron backscatter diffraction (EBSD) was conducted to characterize the materials' microstructure using a TESCAN GAIA3 scanning electron microscope (SEM) equipped with the HKL Channel 5 EBSD system (Oxford Instruments). The EBSD data was analyzed using the OIM^{TM} 8.1 software (EDAX, Inc.).

Crystallographic textures of the materials were further characterized using neutron diffraction at the HIPPO beamline of the Los Alamos Neutron Science Center (LANSCE) with the time-of-flight method using a 10 mm diameter neutron beam from

a tungsten spallation source. Details of the texture measurement at the HIPPO beamline can be found in [23]. Neutron diffraction measurement was conducted using samples with a dimension of 12mm*8mm*5mm. Each sample underwent three different "runs" per measurement, with the sample holder rotating to three distinct positions. The first run was completed in the as-inserted orientation at a defined 0° position. After completion, the sample was then rotated to 67.5° of the original position and further to 90° for two more runs. The purpose of rotating the sample was to obtain additional pole figure coverage. The diffraction data was processed using the Material Analysis Using Diffraction (MAUD) software (Version 2.33) along with the MATLAB plugin MTEX (Version 5.40) to analyze for the texture and generate associated pole figures. More details of the texture data analysis can be found in [24].

Flat dog-bone tensile specimens with the gauge dimension of 18 mm (Length) × 3.4 mm (Width) × 1.4 mm (Thickness) and 18 mm (Length) × 3.4 mm (Width) × 2.0 mm (Thickness) were extracted from the Ti44 and Ti64 bars, respectively. Standard tensile tests were performed on a Zwick-100kN instrument with an extensometer at a constant strain rate of 1.0×10^{-4} s^{-1}. For each material, two tensile specimens were tested.

In addition, we conducted *in situ* tensile tests using the high-energy X-ray diffraction technique at beamline 1-ID of the Advanced Photon Source (APS) at Argonne Nation Laboratory. Tensile specimens with a smaller gauge dimension of 11 mm (Length) × 1.0 mm (Width) × 1.0 mm (Thickness) were extracted from Ti44-V and Ti64-V bars,

with their tensile axes being parallel to the V direction. Tensile tests were carried out using a compact load frame [25] under displacement control with a nominal strain rate of 1×10^{-4} s^{-1}. While each specimen was being continuously deformed, a monochromatic X-ray beam (E=71.68 keV, $\lambda = 0.1730$ Å) with a size of 200 μm × 200 μm probed the gauge center in a transmission geometry. An amorphous Si area detector (GE model 41-RT) was placed approximately 1100 mm away from the specimen to record the diffraction patterns. The detector parameters, such as the beam center and detector tilt angles, were calibrated using a LaB_6 standard sample [26]. More details of the *in situ* test capability of this beamline can be found in [27].

The diffraction patterns were integrated into one-dimensional diffraction profiles using the GSAS-II software [28] over the whole 360° azimuthal range for phase identification purpose, and over ±5° azimuthal range around the tensile loading direction for computing the lattice strains. Each diffraction peak was fitted by a Gaussian function to measure its peak position and full width at half maximum (FWHM). From the evolving diffraction peak positions, lattice strain evolution can be computed as [29, 30]:

$$\varepsilon_{hkl}^{i} = \frac{d_{hkl}^{i}(\sigma) - d_{hkl}^{i}(0)}{d_{hkl}^{i}(0)} \quad (1)$$

where $d_{hkl}^{i}(0)$ and $d_{hkl}^{i}(\sigma)$ are the d-spacing of the {hkl} plane in phase *i* prior to loading and under applied stress σ, respectively.

Microstructures of the as-built materials were further characterized using a Talos F200X G2 transmission electron microscope (TEM). The annular bright field (ABF)

images of dislocations were taken under the two-beam condition using the high angular annular dark field scanning transmission electron microscopy (HAADF-STEM) mode. The TEM samples were prepared by mechanical polishing to a thickness of ~70 μm, followed by twin-jet electro-polishing at -30 °C using a voltage of ~30 V, in a solution of 4% perchloric acid and 96% anhydrous ethanol.

3. Results

3.1 Tensile properties

Fig. 2(a) shows the tensile stress-strain curves of the Ti44-V, Ti44-H, Ti64-V, and Ti64-H specimens. Table 2 shows the average yield strength (YS), ultimate tensile strength (UTS), uniform elongation (ε_u), and fracture elongation (ε_f) values of each material. Ti64-V and Ti64-H specimens exhibit the typical "high-strength, low-ductility" behavior. In contrast, Ti44-V and Ti44-H specimens exhibit lower strength, but significantly improved ductility. Such features were usually observed in LPBF Ti64 after heat treatment under sub-transus temperatures (< 980 ℃) for several hours [6, 31, 32]. Ti64-V has a significantly higher strength but less elongation than Ti64-H, which highlights the anisotropic mechanical behavior for this material. In contrast, the stress-strain curve of Ti44-V was almost identical as Ti44-H, suggesting that the mechanical anisotropy was largely reduced in this new material. We conducted a literature survey of as-built and heat treated LPBF Ti64 to compile the fracture elongation data along both H and V directions (see Table 3). As shown in Fig. 2(b), as-built LPBF Ti44 performs even better than many heat treated LPBF Ti64 in terms of ductility and

isotropy.

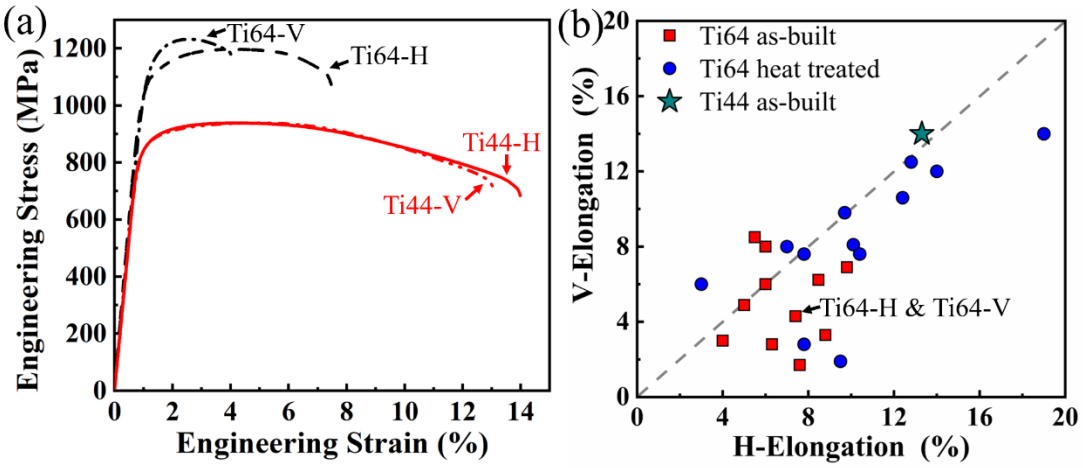

Fig. 2. (a) Tensile stress-strain curves of the Ti44-V, Ti44-H, Ti64-V, and Ti64-H specimens. (b) Fracture elongation along H and V directions of as-built LPBF Ti44 compared to literature values [5, 7, 14, 33–41] of as-built and heat treated LPBF Ti64.

Table 2. Tensile properties of the Ti64-V, Ti64-H, Ti44-V, and Ti44-H specimens.

	YS (MPa)	UTS (MPa)	ε_u (%)	ε_f (%)
Ti64-V	1124±8	1235±3	2.7±0.1	4.3±0.3
Ti64-H	1067±3	1194±4	4.3±0.4	7.4±0.1
Ti44-V	819±18	925±15	5.2±0.3	14±1.0
Ti44-H	836±4	936±3	4.7±0.1	13.3±0.8

Table 3. Tensile properties of LPBF Ti64 in as-built and heat-treated conditions. Air Cool (AC) and Furnace Cool (FC) are the ways of cooling after heat treatment.

Condition	**YS (MPa)**	**UTS (MPa)**	**ε_f (%)**	**Direction**	**Ref.**
as built	1065	1250	4	H	[33]

as built	1060	1090	3	V	[33]
800 °C/2 h/FC	960	1060	19	H	[33]
800 °C/2 h/FC	930	1040	14	V	[33]
as built	1137 ± 20	1206 ± 8	7.6 ± 2	H	[34]
as built	926 ± 47	1116 ± 25	1.7 ± 0.3	V	[34]
730 °C/2 h/AC	965 ± 16	1046 ± 6	9.5 ± 1	H	[34]
730 °C/2 h/AC	900 ± 101	1000 ± 53	1.9 ± 0.8	V	[34]
as built	1075 ± 25	1199 ± 49	9.8 ± 0.5*	H	[35]
as built	967 ± 10	1117 ± 3	6.9 ± 0.4*	V	[35]
730 °C/2 h/FC	974 ± 7	1065 ± 21	10.4 ± 0.7*	H	[35]
730 °C/2 h/FC	937 ± 9	1052 ± 11	7.6 ± 0.9*	V	[35]
as built	1093 ± 64	1279 ± 13	6 ± 0.7	H	[36]
as built	1125 ± 22	1216 ± 8	6 ± 0.4	V	[36]
650 °C/4 h/FC	1145 ± 17	1187 ± 10	7 ± 2.7	H	[36]
650 °C/4 h/FC	1132 ± 13	1156 ± 13	8 ± 0.4	V	[36]
890 °C/2 h/FC	973 ± 8	996 ± 10	3 ± 0.4	H	[36]
890 °C/2 h/FC	964 ± 7	998 ± 14	6 ± 2	V	[36]
as built	1195 ± 19	1269 ± 9	5 ± 0.5	H	[37]
as built	1143 ± 30	1219 ± 20	4.89 ± 0.6	V	[37]
as built	1070 ± 50	1250 ± 50	5.5 ± 1	H	[5]
as built	1050 ± 40	1180 ± 30	8.5 ± 1.5	V	[5]
650 °C/3 h	1010 ± 0.0	1117 ± 1.2	7.8 ± 1.1	H	[38]
650 °C/3 h	1078 ± 2.9	1131 ± 17.4	2.8 ± 0.8	V	[38]
650 °C/3 h	1029 ±8	1091 ±6	7.8 ± 0.8	H	[7]
650 °C/3 h	1161 ± 30	1237 ±30	7.6 ±1	V	[7]
650 °C/3 h	1121 ± 9	1202 ± 11	10.1 ± 0.3	H	[7]
650 °C/3 h	1121 ± 42	1186 ± 42	8.1 ± 0.6	V	[7]
650 °C/3 h	1115 ±18	1183 ±22	9.7 ±0.3	H	[7]

650 °C/3 h	1151 ± 11	1222 ± 25	9.8 ±1.1	V	[7]
650 °C/3 h	1063 ±17	1137 ±23	12.8 ± 0.9	H	[7]
650 °C/3 h	1102 ±16	1145 ±14	12.5 ±1.4	V	[7]
as built	1099	1186	8.47	H	[39]
as built	1185	1293	6.23	V	[39]
as built	1200	1393	6.3	H	[40]
as built	1209	1361	2.8	V	[40]
as built	1047 ± 23	1274 ± 26	6 ± 1*	H	[14]
as built	1043 ± 18	1219 ± 32	8 ± 1*	V	[14]
875–975 °C/24 h/AC (Thermal cycling)	865 ± 19	1017 ± 16	14 ± 1*	H	[14]
875–975 °C/24 h/AC (Thermal cycling)	849 ± 12	1004 ± 23	12 ± 1*	V	[14]
as built	928 ± 4	1171 ± 0	8.8 ± 0.5%*	H	[41]
as built	1023 ± 5	1338 ± 3	3.3 ± 1.4%*	V	[41]
910 °C/4 h/WQ+750 °C/2 h/FC	917 ± 14	1024 ± 4	12.4 ± 0.4%*	H	[41]
910 °C/4 h/WQ+750 °C/2 h/FC	998 ± 8	1063 ± 0	10.6 ± 1.7%*	V	[41]
as built	1069	1197	7.5	H	This work
as built	1117	1232	4.0	V	This work

* In those works, the tensile tests were conducted without an extensometer. The elongation values were corrected based on the given stress-strain curves after removing the artificial elastic elongation part.

3.2 Texture and microstructure characterization

Only diffraction peaks of the α/α′ phase were identified by neutron diffraction. Fig. 3 shows the {0001}, $\{10\bar{1}0\}$, and $\{11\bar{2}0\}$ pole figures for Ti64-V and Ti44-V, as measured by neutron diffraction. The two materials exhibit similarly weak $\{11\bar{2}0\}$ fiber textures, which was also previously reported in [42]. Therefore, the difference in the tensile properties of LPBF Ti64 and Ti44 must be attributed to factors other than the texture.

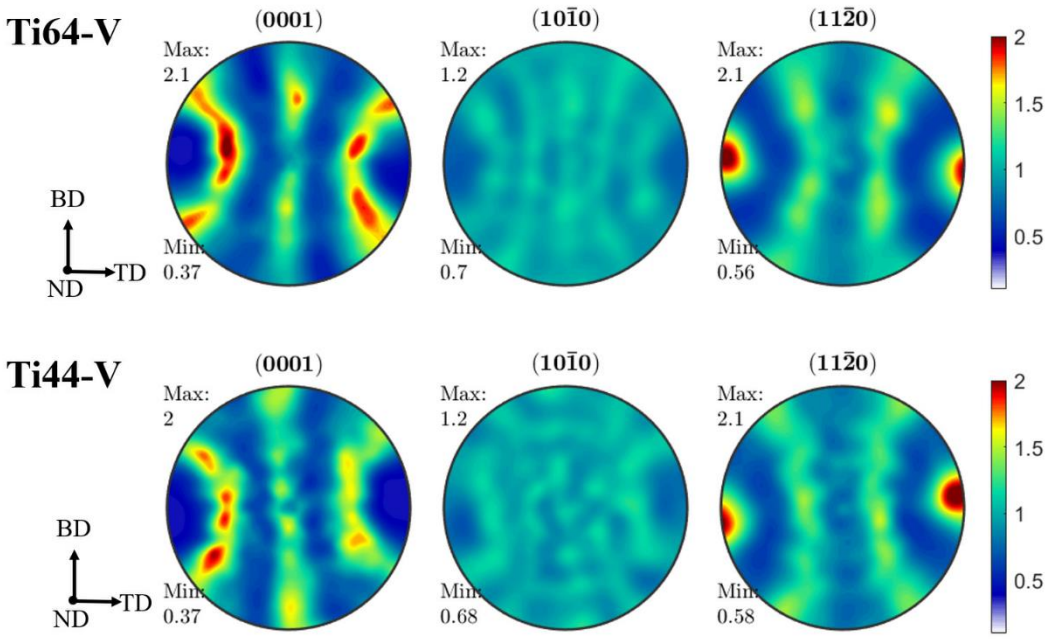

Fig. 3. α/α′ phase texture for the Ti64-V and Ti44-V samples.

Fig. 4 shows optical micrographs of Ti64-V and Ti44-V samples, in which building defects are in dark contrast. We analyzed about 20 optical micrographs for each material, and the porosity values, based on the observed defects, are estimated to be 0.10% and 0.03% for the two materials, respectively. The relatively low porosity indicates that the

building parameters for Ti64 and Ti44 are generally appropriate.

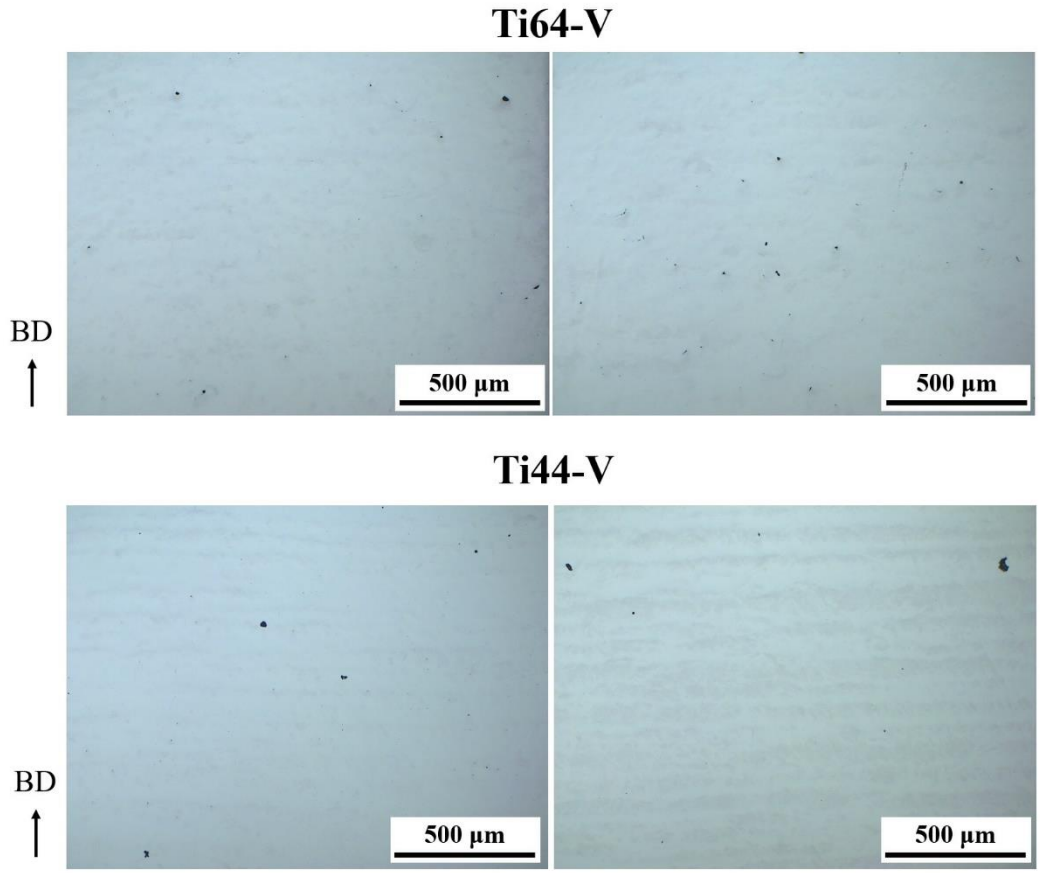

Fig. 4. Optical micrographs showing building defects in Ti64-V and Ti44-V samples.

Microstructures of the as-built Ti64 and Ti44 were characterized by EBSD and shown in Fig. 5. From Fig. 5(a, b), both alloys were dominated by α' laths with small amount of residual β (volume fraction = 0.7% in Ti64; volume fraction = 0.6% in Ti44). The pixels identified as residual β all have confidence index (CI) greater than 0.5. The average width of α' laths in Ti64 and Ti44 are 2.38±1.02 µm and 2.53±1.07 µm, respectively. The average length of α' laths in Ti64 and Ti44 are 16.1±10.4 µm and 14.3±8.5 µm, respectively. Those indexable α' laths are known as the primary martensite [2]. The difference in the morphology of the primary α' laths is relatively

small. It must be pointed out that α' laths with finer scales (width less than 1μm) do exist in the microstructure. They are known as secondary or ternary martensites [2]. These finer laths cannot be indexed by EBSD. We will characterize them using TEM imaging later. The α' laths formed from the martensitic transformation of the prior-β grains during the rapid solidification. We reconstructed the prior-β grains from the crystal orientations of the primary α' laths using the MTEX code [43], and the reconstruction result is shown in Fig. 5(c). The prior-β grains in Ti64 show typical columnar shape, being elongated along the BD. In contrast, the prior-β grains in Ti44 have significantly smaller size as well as reduced aspect ratio than that in Ti64. The scanned areas in Fig. 5(a) are approximately 750 μm × 290 μm for both materials. In this area, about 35 and 97 prior-β grains were identified for Ti64-V and Ti44-V, respectively.

The size of prior-β grains has an impact on the material ductility. Book and Sangid studied the strain localization, precursor for material failure, in heat treated LPBF Ti64 by *in situ* high resolution digital image correlation (HR-DIC) [44]. They found that under tensile loading, strain localizes in long α laths aligned at approximately 45° from the tensile direction. The localized strains in individual α laths are usually impeded at prior-β grain boundaries, which delayed the accumulation of larger strains necessary for crack initiation. When prior-β grains are refined, α laths will be shorter accordingly, so strain localization is going to be mitigated. This mechanism offers an interpretation for the better ductility in Ti44 than in Ti64. Because the prior-β grains in Ti44 are less

columnar, the material also tends to behave more isotropically, as revealed in Fig. 2. The reduction of the size and aspect ratio of prior-β grains is a key feature of the as-built Ti44 alloy, which we will discuss using the solidification theory later.

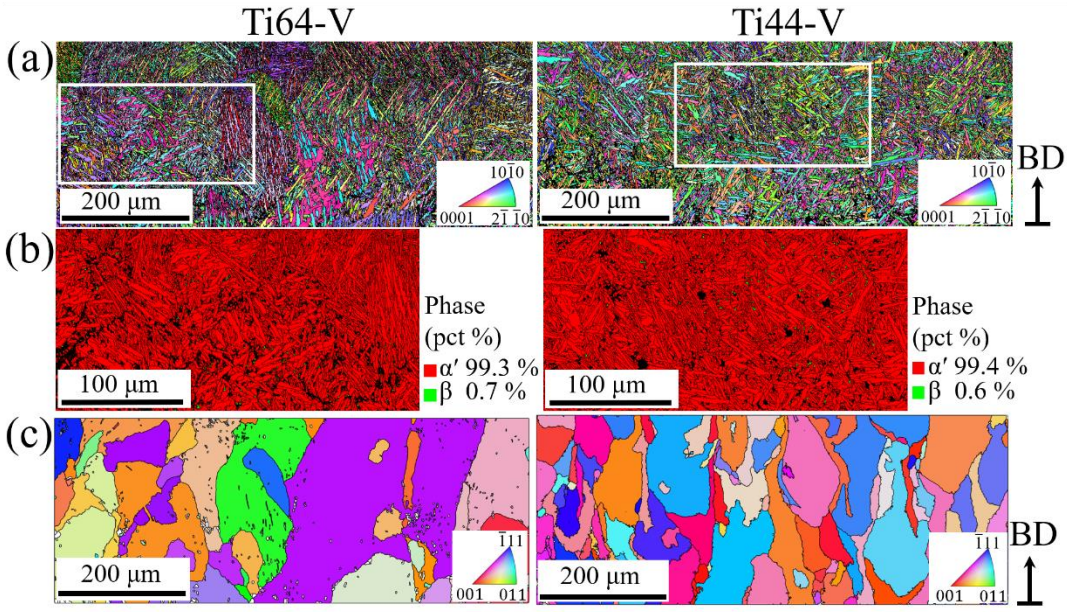

Fig. 5. Comparison of the microstructure of as-built Ti64 and Ti44. (a) EBSD inverse pole figure maps of the α' phase, with the BD as the pole direction. (b) Phase distribution of the white box regions in (a). (c) Inverse pole figure map of the reconstructed prior-β grains from the same area of (a), with the BD as the pole direction.

3.3 In situ HEXRD test

Fig. 6(a) illustrates the setup of the *in situ* HEXRD experiment. The diffraction patterns in the undeformed states and resultant diffraction profiles (integrated over the full 360 deg azimuth range) of Ti64-V and Ti44-V are shown in Fig. 6(b). Both materials show α' peaks only, while β peaks are below the detectable limit. From the indexed peaks, lattice parameters and the c/a ratios are estimated for these two materials: Ti64-V, a=

2.927 Å , c = 4.671 Å , c/a = 1.596; Ti44-V, a = 2.932 Å , c = 4.674 Å , c/a =1.594. Ti44 has slightly smaller c/a ratio than Ti64.

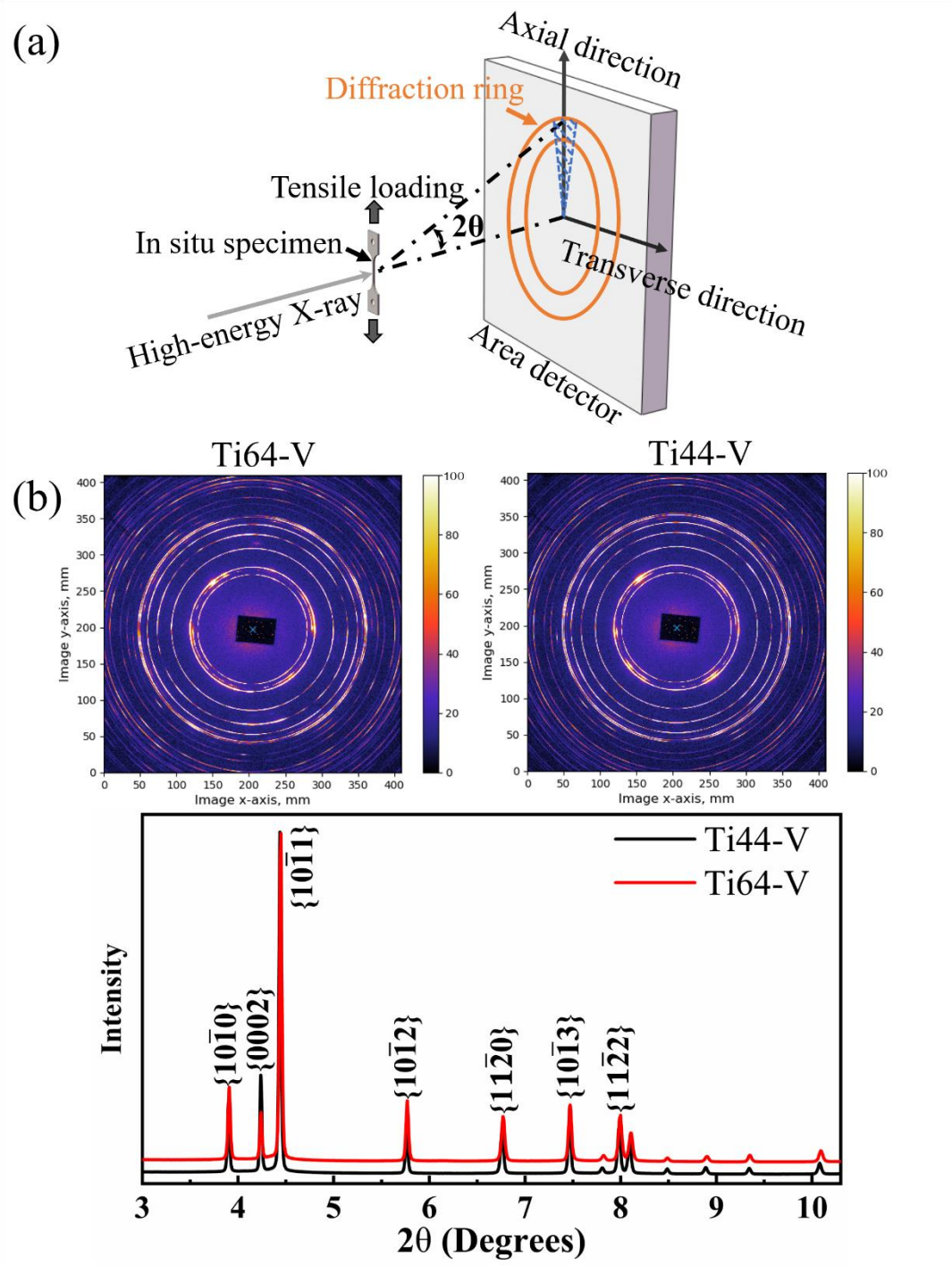

Fig. 6. (a) Schematic of the *in situ* HEXRD test. (b) Diffraction patterns in the undeformed states and the corresponding diffraction profiles of Ti64-V and Ti44-V. Main peaks of the α'/α phase are indexed.

Fig. 7(a) shows the stress-strain curves of Ti64-V and Ti44-V from the *in situ* tensile tests. Like the result in Fig. 2, Ti44-V is less strong but more ductile than Ti64-V. The fracture elongation of Ti44-V is 10.4% from the *in situ* test, which is slightly smaller than the value (ε_f =14±1.0%) from the *ex situ* test. On the other hand, the uniform elongation (ε_u) values are more consistent between the *in situ* test (ε_u=6.5%) and the *ex situ* test (ε_u=5.2±0.3%) for Ti44-V.

Fig. 7(b) shows the lattice strain evolution of $\{10\bar{1}0\}$, $\{10\bar{1}1\}$, and $\{10\bar{1}2\}$ peaks in Ti64-V and Ti44-V during the *in situ* tests. In both specimens, the $\{10\bar{1}0\}$ grain family (grains with one $\{10\bar{1}0\}$ plane being perpendicular to the tensile direction) developed higher lattice strain than the $\{10\bar{1}2\}$ grain family ($\varepsilon_{\{10\bar{1}0\}} > \varepsilon_{\{10\bar{1}2\}}$). Assuming that the grain-level stress is similar to the macroscopic uniaxial stress, this result indicates that basal slip (geometrically favored in the $\{10\bar{1}2\}$ grain family) has lower CRSS than prismatic slip (geometrically favored in the $\{10\bar{1}0\}$ grain family). Lattice strains of the $\{10\bar{1}2\}$ grain family deviated from linearity at 0.0075 for Ti64-V and at 0.0067 for Ti44-V (see the insets in Fig. 7(b)). Lattice strains of the $\{10\bar{1}0\}$ grain family deviated from linearity at 0.010 for Ti64-V and at 0.0080 for Ti44-V. After yielding, $\varepsilon_{\{10\bar{1}0\}}/\varepsilon_{\{10\bar{1}2\}}$ approximately reflects the $CRSS_{prism}/CRSS_{basal}$ ratio [30]. From Fig. 7(b), $CRSS_{prism}/CRSS_{basal}$ is smaller (i.e. closer to 1) in Ti44 (0.0080/0.0067=1.19) than in Ti64 (0.010/0.0075=1.33). Therefore, Ti44 is more likely to activate both basal and prismatic slips during plastic deformation, while Ti64 has to primarily rely on the basal

slip alone. The ability to activate multiple slip modes to satisfy the von Mises criterion (i.e. five independent slip systems) is another reason (in addition to the grain refinement) for the improved ductility in Ti44. We will further explore this issue in the discussion

The diffraction peak broadening was additionally analyzed. Fig. 7(c) shows the FWHM evolution of several peaks in Ti64-V and Ti44-V. FWHM is positively related to the dislocation density, while negatively related to the subgrain size [45, 46]. From Fig. ~~5~~7(c), Ti44 shows less peak broadening than Ti64 at any strain level.

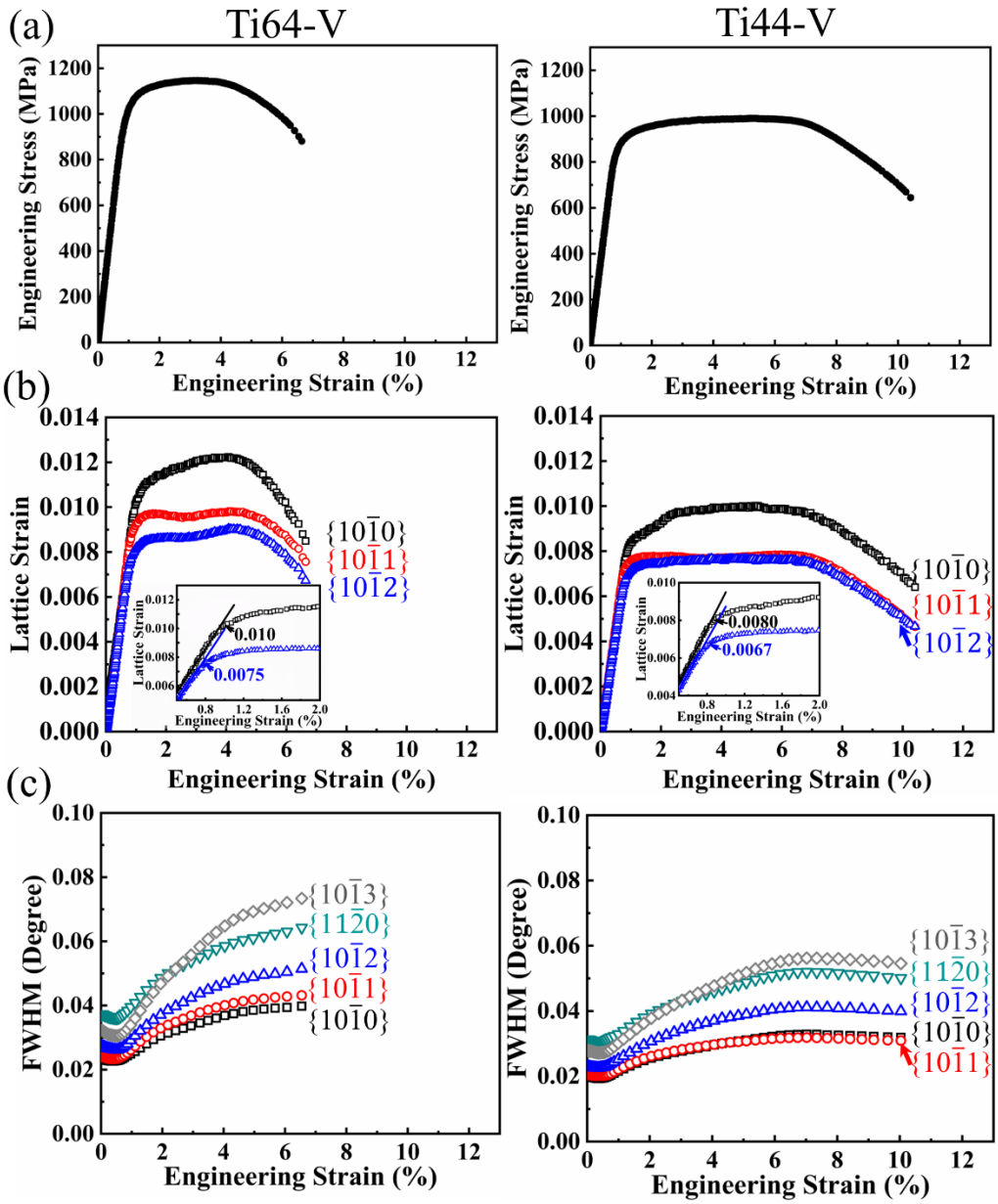

Fig. 7. Results from the *in situ* HEXRD experiment for Ti64-V and Ti44-V. (a) Stress-strain curves. (b) Evolution of the lattice strains of selected α' peaks. (c) Evolution of FWHM of selected α' peaks.

4. Discussion

4.1 Reduction of the prior-β grain size in LPBF Ti44

LPBF Ti44 shows dramatically different microstructure and mechanical properties as compared to LPBF Ti64. First of all, the prior-β grains become significantly smaller and less columnar in Ti44, as revealed in Fig. 5(c). The formation of columnar grains in LPBF is because of the ultrahigh thermal gradient (G ≈ 10^6 to 10^7 K/m) during solidification of laser remelted powders [18]. Since the LPBF Ti64 and Ti44 have similar building parameters, the refinement of β grains in the latter must be attributed to the change of the growth restriction factor Q. For a given solute content, Q is defined by the following equation [47]:

$$\mathrm{Q} = c_0 \cdot m \cdot (k - 1) \tag{2}$$

where *m* is the liquidus slope, *k* is the partition coefficient, and c_0 is the concentration of the element. A larger Q value usually leads to more grain refinement during solidification. When extending the calculation to multicomponent systems, the total value of Q in the multicomponent system can be calculated by adding up the contributions of the binary values of the individual solutes (*i*) [48]:

$$\mathrm{Q} = \sum Q_{bin,i} = \sum c_{0,i} \cdot m_{bin,i} \cdot (k_{bin,i} - 1) \tag{3}$$

For a single binary system, the liquidus slope ($m_{bin,i}$) of the liquidus line (T_L) is calculated by:

$$m_{bin,i} = \frac{dT_L}{dc_{0,i}} \tag{4}$$

The partition coefficient ($k_{bin,i}$) is calculated from the composition of the solid ($c_{S,i}$) and the liquid ($c_{L,i}$) at the given alloy chemistry:

$$k_{bin,i} = \frac{c_{S,i}}{c_{L,i}} \tag{5}$$

Using the Thermo-Calc^{TM} 2021a software in conjunction with the database TCT13 (version 3.0), the equilibrium phase diagrams of Ti-Al and Ti-V were calculated, as shown in Fig. 8. From that, the values of $m_{bin,i}$, $k_{bin,i}$, and Q were computed for Ti-4Al, Ti-6Al, and Ti-4V (Table 4). Using Eq. (3), the values of Q for Ti44 and Ti64 were finally calculated to be 1.830 K and 1.572 K, respectively. Interestingly, the total Q value is increased by reducing Al content in the alloys.

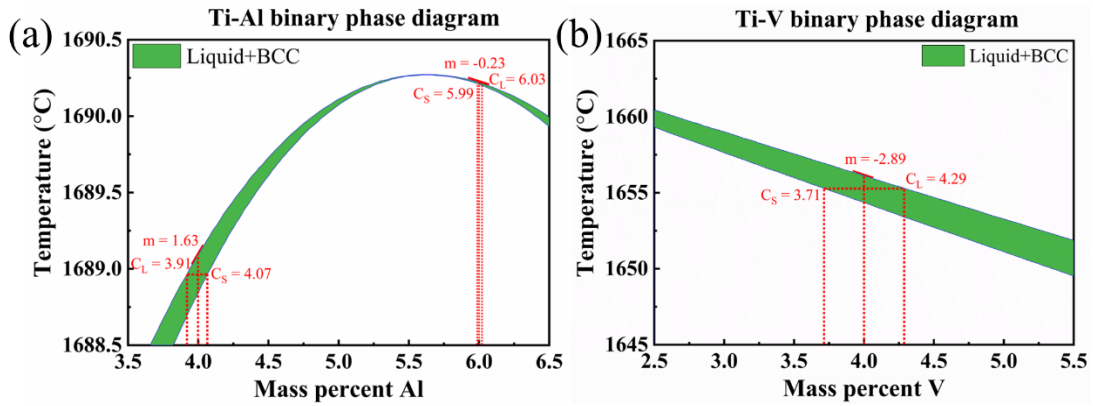

Fig. 8. Binary Ti-Al and Ti-V phase diagrams and the calculation of the liquidus slopes and the partition coefficients.

Table 4. Q values calculated for binary Ti-Al and Ti-V alloys

Alloy	$c_{0,i}$ (wt.%)	$m_{bin,i}$ (wt.%)	$c_{S,i}$ (wt.%)	$c_{L,i}$ (wt.%)	$k_{bin,i}$	$Q_{bin,i}$ (K)
Ti-4Al	4	1.63	4.07	3.91	1.041	0.267
Ti-6Al	6	-0.23	5.99	6.03	0.993	0.009
Ti-4V	4	-2.89	3.71	4.29	0.865	1.563

From the above calculation, Ti44 has a larger Q than Ti64, which can explain the smaller size and aspect ratio of the prior-β grains in LPBF Ti44. To verify this grain

refinement effect by reducing the Al content, we fabricated cast ingots (diameter = 80 mm, thickness =13mm) of Ti-6Al-4V and Ti-4Al-4V (wt.%) by remelting pure Ti (99.9%), pure Al (99.9%), and pure V (99.9%) using vacuum arc melting. As shown in Fig. 9, large columnar grains were found in as-cast Ti64, while as-cast Ti44 contains smaller and more equiaxed grains. The comparison indicates that the reduction of Al content is effective in reducing the size and aspect ratio of prior-β grains in titanium alloys, under both rapid and regular solidification conditions.

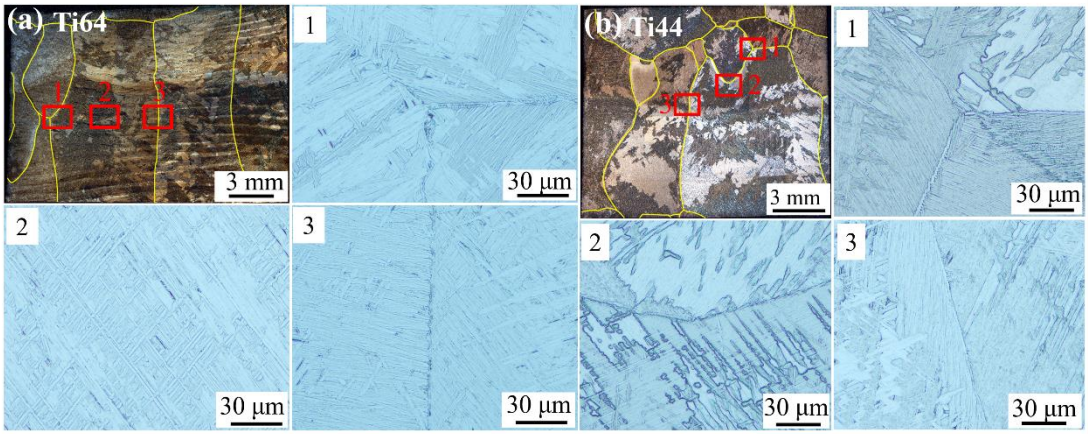

Fig. 9. Optical microscopy of as-cast (a) Ti64 and (b) Ti44. The yellow dashed lines mark the boundary of prior-β grains. Microstructures within the blue boxes are enlarged to show selected regions of grain boundary or grain interior.

We further computed the Q values for Ti-*x*Al-4V (wt.%) using the above method, with *x* ranging from 2 to 8. As shown in Fig. 10, the minimum Q value is found at *x*=6. It implies that although Ti-6Al-4V is the mostly used wrought titanium alloy, it's chemical composition would inevitably lead to large columnar grains. Adjusting the Al content is a simple solution to induce a partial columnar to equiaxed transition (CET). The

change in the morphology of prior-β grains can explain the improved ductility in LPBF Ti44.

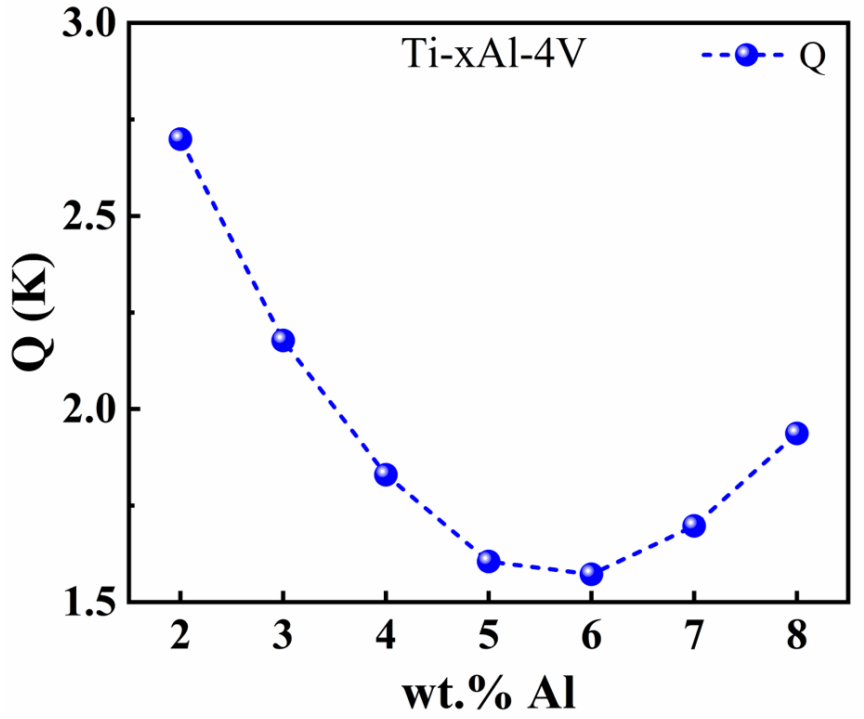

Fig. 10. Q values of Ti-*x*Al-4V (*x*=2~8 wt.%) alloys.

4.2 Dislocation activity and improved ductility in LPBF Ti44

In Ti-Al alloys, the Al addition increases the c/a ratio in Ti, which increases the basal plane spacing while reduces the prismatic plane spacing [21]. As a result, basal slip is favored over prismatic slip. This effect seems to hold for the LPBF Ti alloys. The c/a ratio of the LPBF Ti44 (c/a=1.594) is smaller than that of the LPBF Ti64 (c/a=1.596). This offers an explanation on the smaller $CRSS_{prism}/CRSS_{basal}$ ratio in LPBF Ti44 (~1.19) than that in LPBF Ti64 (~1.33).

Increasing Al content also leads to more planar slip in Ti (i.e. difficulty for cross-slip between basal and prismatic planes) [22]. To study this aspect, we characterize the dislocations in as-built Ti64-V and Ti44-V using TEM. The results are presented in Fig. 11.

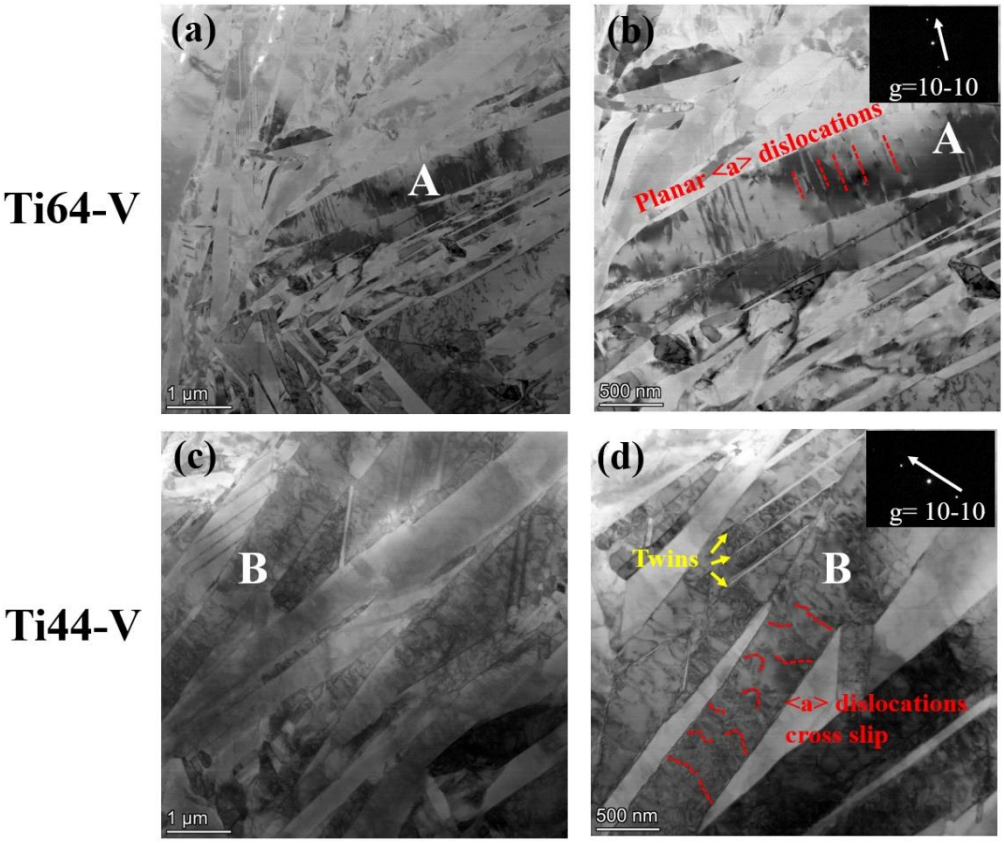

Fig. 11. Bright field images of (a) Ti64-V and (c) Ti44-V using the HAADF-STEM mode. (b) Higher magnification image taken at the two-beam condition for Grain A from a zone axis of $[1\bar{2}1\bar{3}]$ with **g**=$(10\bar{1}0)$. (d) Higher magnification image taken at the two-beam condition for Grain B from a zone axis of $[\bar{2}4\bar{2}3]$ with **g**=$(10\bar{1}0)$.

Acicular α′ martensite laths with sub-micron width are observed in both Ti64 and Ti44. They are the so-called secondary α′ martensite [2]. From Fig. ~~6~~11(a, c), the average

width of the secondary α′ martensite laths in Ti64 and Ti44 are approximately 0.3μm and 0.7μm, respectively. Dislocations in Grain A of Ti64 and Grain B of Ti44 were further imaged using the two-beam condition and shown in Fig. ~~6~~11(b, d). With **g**=$(10\bar{1}0)$ in both cases, dislocations in both grains are mainly the <a> type. In Grain A of Ti64, dislocations are planar. In Grain B of Ti44, many dislocations are curved, suggesting extensive cross-slip, presumably between basal and prismatic planes. This result agrees with a recent investigation of the dislocation morphology in deformed Ti-xAl-0.1O (wt.%) alloys (x=0, 2, 4, and 6), where samples with higher Al content show planar slip while samples with lower Al content show more cross slip [49]. Deformation twins are also observed in Ti44 (Fig. 11(d)) but not in Ti64. Dislocations and twins form in martensite laths of LPBF Ti alloys to accommodate the phase transformation strain from β to α′. It is reasonable to assume that the dislocation morphology and twinning activity in as-built Ti64 and Ti44 will also hold for their plastic deformation. Therefore, the high ductility in LPBF Ti44 may also be attributed to the enhanced cross-slip and twinning due to the reduction of Al content.

4.3 Understanding the reduced strength in LPBF Ti44

While LPBF Ti44 shows better ductility and mechanical isotropy, its yield strength is much lower than LPBF Ti64. The yield strength of metals can usually be written as following:

$$\sigma_{YS} = \sigma_0 + \sigma_{ss} + \frac{k_{HP}}{\sqrt{d}} + \sigma_{dis} \quad (6)$$

where σ_0 is the friction stress, σ_{ss} is the solid solution strengthening, k_{HP} is the Hall-Petch coefficient (taken as 223 MPa·μm$^{-1/2}$ according to Ref. [50]), d is the grain size, and σ_{dis} is the dislocation strengthening.

The yield strength (~270 MPa) of a hot-rolled Ti-0.1wt.%O material with an equiaxed grain size of 60 μm [49] was used to compute σ_0:

$$\sigma_0 = 270\ \text{MPa} - \frac{k_{HP}}{\sqrt{60\mu m}} = 241\ MPa \quad (7)$$

The solid solution strengthening was calculated using the Labusch's approach [51]:

$$\sigma_{ss} = \left(\sum_i B_i^{3/2} x_i\right)^{2/3} \quad (8)$$

where x_i is the atomic concentration of element i, B_i is a strengthening constant of element i in Ti. B_{Al} and B_V are 1813 MPa/at$^{2/3}$ and 127 MPa/at$^{2/3}$, respectively [52]. The solid solution strengthening (σ_{ss}) of Ti64 (x_{Al}=0.1045, x_V=0.0421) and Ti44 (x_{Al}=0.0676, x_V=0.0416) are thus calculated to be 404 MPa and 303 MPa, respectively.

Using d = 0.3μm and 0.7μm for Ti64 and Ti44, the Hall-Petch strengthening ($\frac{k_{HP}}{\sqrt{d}}$) for Ti64 and Ti44 are 407 MPa and 266 MPa, respectively.

The dislocation strengthening is described by the following formula:

$$\sigma_{dis} = M\alpha_\rho G b\sqrt{\rho_0} \quad (9)$$

where M is the Taylor factor (taken as 3), α_ρ is a coefficient (taken as 0.3), G is the shear modulus of α′ (43.3 GPa) [50], b is the Burgers vector length (=0.295nm), and ρ_0 is the initial dislocation density. ρ_0 is estimated by the net strain energy accommodated by

dislocations in a single martensite lath [50], as expressed by:

$$\rho_0 = \frac{12Es}{(1+2v^2)Gb}\frac{\varepsilon_{trans}^2}{d^2} \quad (10)$$

where E and G are the Young's modulus and shear modulus of α' (113 GPa and 43.3 GPa), s is the lath boundary thickness (taken as 10 nm), v is the Poisson's ratio (~0.34), and ε_{trans} is the transformation strain from β to α' (~0.1) [50].

Using d = 0.3μm and 0.7μm for Ti64 and Ti44, the initial dislocation density for LPBF Ti64 and Ti44 are approximately 2.87×10^{13} m^{-2} and 0.52×10^{13} m^{-2}, respectively. Using Eq. (9), the dislocation strengthening (σ_{dis}) for Ti64 and Ti44 are 64 MPa and 27 MPa, respectively.

Table 5 summarizes the contribution of each strengthening mechanism and the theoretical yield strength using Eq. (6) for Ti64-V and Ti44-V. The values are close to the measured yield strength for these two materials. The low strength in LPBF Ti44 mostly results from the less solid strengthening and the larger width of the secondary α′ laths.

Table 5 Contribution of each strengthening mechanism and the theoretical and measured yield strength for Ti64-V and Ti44-V. The units are MPa.

	σ_0	σ_{ss}	$\frac{k_{HP}}{\sqrt{d}}$	σ_{dis}	σ_{YS} *(theory)*	σ_{YS} *(measured)*
Ti64-V	241	404	407	64	1116	1124±8
Ti44-V	241	303	266	27	837	819±18

5. Conclusions

In this work, we designed a new titanium alloy (Ti44) with reduced Al content for laser powder bed fusion. Its tensile properties, microstructure, and deformation mechanisms were characterized. The main conclusions are summarized below:

(1) In contrast to the typical formation of columnar prior-β grains in LPBF Ti64, LPBF Ti44 shows reduced prior-β grain size and aspect ratio. This observation can be interpreted from the calculation of the growth restriction factor Q. The change in the prior-β grain morphology leads to mechanical isotropy in LPBF Ti44.

(2) With the reduced Al content, the $CRSS_{prism}/CRSS_{basal}$ ratio becomes lower in LPBF Ti44, and dislocation cross-slip and twinning become easier. The change in the dislocation and twinning activity improves the ductility in LPBF Ti44.

(3) LPBF Ti44 exhibits lower strength, owing to the reduced solid solution hardening and the ~~layer~~ larger width of the secondary α' laths.

Taken together, this work points out a new strategy to improve the mechanical properties of LPBF titanium alloys by tailoring the Al content. This strategy can open up new opportunities for the industrial applications of the LPBF technique.

Acknowledgments

The materials used for this study were fabricated by the Falcontech company. We thank

Prof. Marko Knezevic for the assistance in neutron diffraction texture measurement. This work is financially supported by the National Natural Science Foundation of China (Nos. U2032124, 51631006, and 51825101). Use of the Advanced Photon Source was supported by the United States Department of Energy, Office of Science, Office of Basic Energy Sciences, under Contract No. DE-AC02-06CH11357.

References

[1] T. DebRoy, H.L. Wei, J.S. Zuback, T. Mukherjee, J.W. Elmer, J.O. Milewski, A.M. Beese, A. Wilson-Heid, A. De, W. Zhang, Additive manufacturing of metallic components – Process, structure and properties. Prog. Mater. Sci. 92 (2018) 112-224.

[2] J. Yang, H. Yu, J. Yin, M. Gao, Z. Wang, X. Zeng, Formation and control of martensite in Ti-6Al-4V alloy produced by selective laser melting. Materials & Design. 108 (2016) 308-318.

[3] H. Shipley, D. McDonnell, M. Culleton, R. Coull, R. Lupoi, G. O'Donnell, D. Trimble, Optimisation of process parameters to address fundamental challenges during selective laser melting of Ti-6Al-4V: A review. International Journal of Machine Tools and Manufacture, 128 (2018) 1-20.

[4] G. Lütjering, J.C. Williams, Engineering materials and processes: titanium, 2nd ed., Springer, New York, 2007

[5] C. Qiu, N.J.E. Adkins, M.M. Attallah, Microstructure and tensile properties of selectively laser-melted and of HIPed laser-melted Ti–6Al–4V. Mater. Sci. Eng. A 578 (2013) 230-239.

[6] B. Vrancken, L. Thijs, J.-P. Kruth, J. Van Humbeeck, Heat treatment of Ti6Al4V produced by Selective Laser Melting: Microstructure and mechanical properties. J. Alloy Compd. 541 (2012) 177-185.

[7] P. Kumar, O. Prakash, U. Ramamurty, Micro-and meso-structures and their influence on mechanical properties of selectively laser melted Ti-6Al-4V. Acta Mater.

154 (2018) 246-260.

[8] J.J. Lewandowski, M. Seifi, Metal Additive Manufacturing: A Review of Mechanical Properties. Annu. Rev. Mater. Res. 46 (2016) 151-186.

[9] W. Xu, M. Brandt, S. Sun, J. Elambasseril, Q. Liu, K. Latham, K. Xia, M. Qian, Additive manufacturing of strong and ductile Ti-6Al-4V by selective laser melting via in-situ martensite decomposition. Acta Mater. 85 (2015) 74-84.

[10] W. Xu, E.W. Lui, A. Pateras, M. Qian, M. Brandt, In situ tailoring microstructure in additively manufactured Ti-6Al-4V for superior mechanical performance. Acta Mater. 125 (2017) 390-400.

[11] A. Zafari, M.R. Barati, K. Xia, Controlling martensitic decomposition during selective laser melting to achieve best ductility in high strength Ti-6Al-4V. Mater. Sci. Eng. A 744 (2019) 445-455.

[12] P. Barriobero-Vila, J.M. Vallejos, J. Gussone, J. Haubrich, K. Kelm, A. Stark, N. Schell, G. Requena, Interface-Mediated Twinning-Induced Plasticity in a Fine Hexagonal Microstructure Generated by Additive Manufacturing. Advanced Materials 33 (2021) 2105096.

[13] Z. Zhao, J. Chen, H. Tan, G. Zhang, X. Lin, W. Huang, Achieving superior ductility for laser solid formed extra low interstitial Ti-6Al-4V titanium alloy through equiaxial alpha microstructure. Scripta Mater. 146 (2018) 187-191.

[14] R. Sabban, S. Bahl, K. Chatterjee, S. Suwas, Globularization using heat treatment in additively manufactured Ti-6Al-4V for high strength and toughness. Acta Mater. 162 (2019) 239-254.

[15] K. Zhang, X. Tian, M. Bermingham, J. Rao, Q. Jia, Y. Zhu, X. Wu, S. Cao, A. Huang, Effects of boron addition on microstructures and mechanical properties of Ti-6Al-4V manufactured by direct laser deposition. Materials & Design. 184 (2019) 108191.

[16] M.Y. Mendoza, P. Samimi, D.A. Brice, B.W. Martin, M.R. Rolchigo, R. LeSar, P.C. Collins, Microstructures and Grain Refinement of Additive-Manufactured Ti-xW Alloys. Metall. Mater. Trans. A 48 (2017) 3594-3605.

[17] D. Zhang, D. Qiu, M.A. Gibson, Y. Zheng, H.L. Fraser, D.H. StJohn, M.A. Easton, Additive manufacturing of ultrafine-grained high-strength titanium alloys. Nature 576 (2019) 91-95.

[18] M. Simonelli, D.G. McCartney, P. Barriobero-Vila, N.T. Aboulkhair, Y.Y. Tse, A. Clare, R. Hague, The Influence of Iron in Minimizing the Microstructural Anisotropy of Ti-6Al-4V Produced by Laser Powder-Bed Fusion. Metall. Mater. Trans. A, 51 (2020) 2444-2459.

[19] P.C. Collins, D.A. Brice, P. Samimi, I. Ghamarian, H.L. Fraser, Microstructural Control of Additively Manufactured Metallic Materials. Annu. Rev. Mater. Res., 46(2016) 63–91.

[20] D. Zhang, A. Prasad, M.J. Bermingham, C.J. Todaro, M.J. Benoit, M.N. Patel, D. Qiu, D.H. StJohn, M. Qian, M.A. Easton, Grain Refinement of Alloys in Fusion-Based Additive Manufacturing Processes. Metall. Mater. Trans. A 51 (2020) 4341-4359.

[21] J.C. Williams, R.G. Baggerly, N.E. Paton, Deformation behavior of HCP Ti-Al alloy single crystals. Metall. Mater. Trans. A 33 (2002) 837-850.

[22] R. Zhang, S. Zhao, C. Ophus, Y. Deng, S.J. Vachhani, B. Ozdol, R. Traylor, K.C. Bustillo, J.W. Morris, D.C. Chrzan, M. Asta, A.M. Minor, Direct imaging of short-range order and its impact on deformation in Ti-6Al. Science Advances. 5 (2019) eaax2799.

[23] H.R. Wenk, L. Lutterotti, S. Vogel, Texture analysis with the new HIPPO TOF diffractometer. Nucl. Instr. Meth. Phys. Res. 515 (2003) 575-588.

[24] A.I. Saville, A. Creuziger, E.B. Mitchell, S.C. Vogel, J.T. Benzing, J. Klemm‐Toole,

K.D. Clarke, A.J. Clarke, MAUD Rietveld Refinement Software for Neutron Diffraction Texture Studies of Single- and Dual-Phase Materials. Integr Mater Manuf Innov. 10 (2021) 461-487.

[25] L. Wang, Z. Huang, H. Wang, A. Maldar, S. Yi, J.-S. Park, P. Kenesei, E. Lilleodden, X. Zeng, Study of slip activity in a Mg-Y alloy by in situ high energy X-ray diffraction microscopy and elastic viscoplastic self-consistent modeling. Acta Mater,

155 (2018) 138-152.

[26] D.R. Black, D. Windover, A. Henins, J. Filliben, J.P. Cline, Certification of Standard Reference Material 660B. Powder Diffraction 26 (2012) 155-158.

[27] J.-S. Park, J. Okasinski, K. Chatterjee, Y. Chen, J. Almer, Non-Destructive Characterization of Engineering Materials Using High-Energy X-rays at the Advanced Photon Source. Synchrotron Radiation News 30 (2017) 9-16.

[28] B.H. Toby, R.B. Von Dreele, GSAS-II: the genesis of a modern open-source all purpose crystallography software package. J. Appl. Crystallogr. 46 (2013) 544-549.

[29] J. Wang, L. Wang, G. Zhu, B. Zhou, T. Ying, X. Zhang, Q. Huang, Y. Shen, X. Zeng, H. Jiang, Understanding the High Strength and Good Ductility in LPSO-Containing Mg Alloy Using Synchrotron X-ray Diffraction. Metall. Mater. Trans. A 49 (2018) 5382-5392.

[30] D. Zhang, L. Wang, H. Zhang, A. Maldar, G. Zhu, W. Chen, J.-S. Park, J. Wang, X. Zeng, Effect of heat treatment on the tensile behavior of selective laser melted Ti-6Al-4V by in situ X-ray characterization. Acta Mater. 189 (2020) 93-104.

[31] P. Kumar, U. Ramamurty, Microstructural optimization through heat treatment for enhancing the fracture toughness and fatigue crack growth resistance of selective laser melted Ti6Al4V alloy. Acta Mater. 169 (2019) 45-59.

[32] Z. Zou, M. Simonelli, J. Katrib, G. Dimitrakis, R. Hague, Microstructure and tensile properties of additive manufactured Ti-6Al-4V with refined prior-β grain structure obtained by rapid heat treatment. Mater. Sci. Eng. A 814 (2021) 141271.

[33] S. Cao, Z. Chen, C.V.S. Lim, K. Yang, Q. Jia, T. Jarvis, D. TOMUS, X. Wu, Defect, microstructure, and mechanical property of Ti-6Al-4V alloy fabricated by high-power selective laser melting. JOM. 69 (2017) 2684-2692.

[34] T. Vilaro, C. Colin, J.D. Bartout, As-fabricated and heat-treated microstructures of the Ti-6Al-4V alloy processed by selective laser melting. Metall. Mater. Trans. A. 42 (2011) 3190-3199.

[35] M. Simonelli, Y.Y. Tse, C. Tuck, Effect of the build orientation on the mechanical properties and fracture modes of SLM Ti-6Al-4V. Mater. Sci. Eng. A. 616 (2014) 1-11.

[36] V. Cain, L. Thijs, J.V. Humbeeck, B.V. Hooreweder, R. Knutsen. Crack propagation and fracture toughness of Ti-6Al-4V alloy produced by selective laser melting. Addit. Manuf. 5 (2015) 68-76.

[37] H.K. Rafi, N.V. Karthik, H. Gong, T.L. Starr, B.E. Stucker. Microstructures and mechanical properties of Ti6Al4V parts fabricated by selective laser melting and electron beam melting. J. Mater. Eng. Perform. 22 (2013) 3872-3883.

[38] A.E. Wilson-Heid, Z. Wang, B. McCornac, A.M. Beese, Quantitative relationship between anisotropic strain to failure and grain morphology in additively manufactured Ti-6Al-4V. Mater. Sci. Eng. A. 706 (2017) 287-294.

[39] S. Palanivel, A.K. Dutt, E.J. Faierson, R.S. Mishra, Spatially dependent properties in a laser additive manufactured Ti-6Al-4V component. Mater. Sci. Eng. A. 654 (2016) 39-52.

[40] A.D. Baghi, S. Nafsi, R. Hashemi, H. Ebendorff-Heidepriem, R. Ghomashchi, Experimental realisation of build orientation effects on the mechanical properties of truly as-built Ti-6Al-4V SLM parts. J. Manuf. Process. 64 (2021) 140-152.

[41] M. Fang, F. Hu, Y. Han, J. Le, J. Xi, J. Song, L. Ke, M. Xiao, W. Lu, Controllable mechanical anisotropy of selective laser melted Ti6Al4V: A new perspective into the effect of grain orientations and primary grain structure. Mater. Sci. Eng. A 827 (2021) 142031.

[42] A. Pesach, E. Tiferet, S.C. Vogel, M. Chonin, A. Diskin, L. Zilberman, O. Rivin, O. Yeheskel, E.N. Caspi, Texture analysis of additively manufactured Ti-6Al-4V using neutron diffraction. Additive Manufacturing. 23 (2018) 394-401.

[43] F. Niessen, T. Nyyssönen, A. A. Gazder, R. Hielscher. Parent grain reconstruction from partially or fully transformed microstructures in MTEX. (2021) http://arxiv.org/abs/2104.14603

[44] T.A. Book, M.D. Sangid, Strain localization in Ti-6Al-4V Widmanstätten microstructures produced by additive manufacturing. Materials Characterization, 122 (2016) 104-112.

[45] T. Ungár, S. Ott, P.G. Sanders, A. Borbély, J.R. Weertman, Dislocations, grain size

and planar faults in nanostructured copper determined by high resolution X-ray diffraction and a new procedure of peak profile analysis. Acta Mater. 46 (1998) 3693-3699.

[46] L.Y. Wang, M.M. Li, J. Almer, Investigation of deformation and microstructural evolution in Grade 91 ferritic-martensitic steel by in situ high-energy X-rays. Acta Mater. 62 (2014) 239-249.

[47] D.H. StJohn, M. Qian, M.A. Easton, P. Cao, Z. Hildebrand, Grain refinement of magnesium alloys. Metall. Mater. Trans. A 36 (2005) 1669-1679.

[48] R.Schmid-Fetzer, A.Kozlov, Thermodynamic aspects of grain growth restriction in multicomponent alloy solidification. Acta Mater. 59 (2011) 6133-6144.

[49] Y. Chong, R. Zhang, M.S. Hooshmand, S. Zhao, D.C. Chrzan, M. Asta, J.W. Morris, A.M. Minor, Elimination of oxygen sensitivity in α-titanium by substitutional alloying with Al. Nat. Commun. 12 (2021) 6158.

[50] X. Yang, R. A. Barrett, N. M. Harrison, S. B. Leen. A physically-based structure-property model for additively manufactured Ti-6Al-4V. Materials & Design 205 (2021) 109709.

[51] R. Labusch, A statistical theory of solid solution hardening. Phys. Status Solidi B 41 (1970) 659-669.

[52] M.A. Galindo-Fernández, K. Mumtaz, P.E.J. Rivera-Díaz-del-Castillo, E.I. Galindo-Nava, H. Ghadbeigi, A microstructure sensitive model for deformation of Ti-6Al-4V describing Cast-and-Wrought and Additive Manufacturing morphologies. Materials & Design, 160 (2018) 350-362.